

A new semi-coherent targeted search for continuous gravitational waves from pulsars in binary systems

L. Mirasola,^{2,4, a} P. Leaci,^{1,3} P. Astone,³ L. D’Onofrio,³ S. Dall’Osso,^{1,3} A. De Falco,^{2,4}
M. Lai,⁵ S. Mastrogiovanni,³ C. Palomba,³ A. Riggio,^{2,4,6} and A. Sanna^{2,4}

¹*Physics Department, Università di Roma “Sapienza”, P.le A. Moro, 2, I-00185 Roma, Italy*

²*Physics Department, Università degli Studi di Cagliari, Cagliari 09042, Italy*

³*INFN, Sezione di Roma, P.le A. Moro, 2, I-00185 Roma, Italy*

⁴*INFN, Sezione di Cagliari, Cagliari 09042, Italy*

⁵*Department of Physics and Astronomy, University of California, Riverside, CA 92521, USA*

⁶*INAF/IASF Palermo, via Ugo La Malfa 153, I-90146 - Palermo, Italy*

We present a novel semi-coherent targeted search method for continuous gravitational waves (CWs) emitted by pulsars in binary systems. The method is based on a custom optimization of the coherence time according to the orbital parameters and their uncertainties, as provided by electromagnetic observations. While rotating pulsars are expected to produce quasi-monochromatic CWs in their reference frame, their orbital motion introduces an additional modulation in the observer frame, alongside the one due to the Earth’s motion. As a result, the received signal is dispersed across a frequency range and demodulation techniques must be used to improve sensitivity. However, Doppler corrections can, in some cases, significantly vary within the uncertainties of orbital parameters, potentially lowering the detection chances of single-template fully-coherent searches. In order to exploit the constraints drawn from electromagnetic observations we implement a semi-coherent search, more robust than these other methods, in which the coherence time is evaluated for each source taking into account uncertainties in its orbital parameters. This method was tested and applied to a set of twelve targets from the ATNF catalogue. The search identified one outlier whose astrophysical origin has been confidently excluded. For the first time to our knowledge, we then set upper limits on the signal strain from these 12 pulsars, the lowest being $h_{UL} \sim 9.01 \times 10^{-26}$ for PSR J1326-4728B.

I. INTRODUCTION

While $\mathcal{O}(10^8 - 10^9)$ neutron stars (NSs) are thought to exist in our Galaxy [1], only a few thousand have been observed thanks to their electromagnetic (EM) emission. Most of these are rotation-powered radio pulsars whose emission beam points along our line-of-sight, while a fraction is known from their broadband emission, which can be powered by accretion, dissipation of magnetic energy or even residual thermal energy [2]. Besides their EM emission, rotating NSs are expected to radiate Continuous gravitational Waves (CWs) if a shape asymmetry is present. CW emission is essentially monochromatic in the NS reference frame and can be driven by elastic, thermal, or magnetic anisotropic stresses in the NS crust or core [3], or from a mass-current quadrupole induced by core fluid instabilities like, e.g., the r -modes [4]. Detecting CW signals will therefore allow us to determine the NS mass quadrupole, hence its degree of asymmetry, and eventually get insights on the NS interior structure as well as on the equation of state (EoS) of matter at supra-nuclear density (see, e.g. [5] and references herein).

All-sky searches for CWs represent to date the only means by which we can unveil the huge population of undetected NS in the Galaxy. These all-sky searches for CWs have already been carried out in Advanced LIGO and Advanced Virgo data from previous science runs, leading to upper limits on the Gravitational Wave (GW) signal strain from NS in the galactic population both for isolated stars (e.g., [6–14]), and in binary systems (e.g., [15–18]).

On the other hand, the EM emission of known NSs, both isolated and in binary systems, provides accurate measurements of their sky location, rotational and, eventually, binary orbital parameters. For these sources, searches have been performed looking for a corresponding CW signal (e.g., [19–32]), either using a single-template approach (targeted) or rather exploring a limited range around the known parameters (narrow-band or directed).

In this work we present a novel approach to targeted searches of CWs from known pulsars in binary systems. Uncertainties on the orbital parameters for such systems can sometimes affect the accuracy of Doppler corrections leading to a loss of Signal-to-Noise Ratio (SNR) [33] if not considered. To tackle this problem, we adopt a semi-coherent technique in which data are first divided into segments, each of which is analyzed coherently before all segments are finally re-combined incoherently. Semi-

^a mail to lorenzo.mirasola@ca.infn.it

coherent methods are less sensitive but more robust than single-segment analyses, as they do not rely on a strict phase-coherence of the signal over extended time spans (NSs CW emission can be affected by stochastic processes such as glitches [34] or accretion-induced spin wandering [35]). The novelty of our method is to choose a customised length of the segments according to the combined uncertainty of the neutron star binary orbital parameters. In this way, we can perform a single-template search and reduce the potential significance loss, even with some reduction in sensitivity.

The method has been tested and applied to a subset of pulsars from the ATNF catalogue¹ (version 1.70) using O3 data². Although throughout this paper we exploit only our new semi-coherent method, the coherence time calculation highlighted a fraction of the targets for which a full-coherent single-template approach could be safely applied without the need for a grid. Future searches can, in principle, make use of our coherence time calculation to decide whether a single- or multi-template search is needed for a given ephemeris.

The plan of the paper is as follows: Sec. II describes the adopted phase model for the GW signal, used to remove the Doppler modulation due to the relative motion between the star and detector. Sec. III lists the selection criteria of the chosen pulsars in binary systems as extracted from the ATNF catalogue. Sec. IV outlines the analysis method, together with its validation. A thorough discussion of the results is provided in Sec. V, which also presents the upper limit calculation that we performed. Sec. VI summarises our results and their relevance for future searches, as well as discusses possible future developments.

II. THE EXPECTED SIGNAL

Here, we briefly describe the expected CW signal from a rotating NS, either isolated or in a binary system.

A. Isolated neutron star phase

The signal strain from a non-axis-symmetric NS, which is rotating around one of its principal axes,

can be expressed in the detector reference frame [41] as

$$h(t) = h_0 F_+(t; \vec{n}, \Psi) \frac{1 + \cos^2 \iota}{2} \cos \phi(t) + h_0 F_\times(t; \vec{n}, \Psi) \cos \iota \sin \phi(t), \quad (1)$$

where ϕ represents the GW phase (including modulations from the Earth motion) and ι the inclination angle of the NS rotational axis with respect to the line of sight; $F_{+, \times}$ are the time-dependent beam pattern functions [41] that encode the detector response as a function of the source sky position \vec{n} , and of the polarization angle Ψ . The CW amplitude is defined for a quadrupolar deformation as

$$h_0 = \frac{4\pi^2 G}{c^4} \frac{I_{zz} \varepsilon f_0^2}{d}, \quad (2)$$

where $\varepsilon = (I_{xx} - I_{yy})/I_{zz}$ is the equatorial ellipticity and f_0 the signal frequency, i.e., the time derivative of ϕ over 2π evaluated at a certain reference time t_{ref} , which for rotating asymmetric NS is expected to be twice the rotational frequency, namely $f_0 = 2 f_{\text{rot}}$.

Eq. (1) can be expressed as the real part of [42]

$$h(t) = H_0 (A^+ H_+ + A^\times H_\times) e^{j\phi(t)}, \quad (3)$$

where $A^{+/\times} = F^{+/\times}(t; \vec{n}, 0)$, and

$$H_0 = \frac{h_0}{2} \sqrt{1 + 6 \cos^2 \iota + \cos^4 \iota}, \quad (4)$$

$$H_+ = \frac{\cos 2\Psi - j \eta_{\text{pol}} \sin 2\Psi}{\sqrt{1 + \eta_{\text{pol}}^2}}, \quad (5)$$

$$H_\times = \frac{\sin 2\Psi + j \eta_{\text{pol}} \cos 2\Psi}{\sqrt{1 + \eta_{\text{pol}}^2}}, \quad (6)$$

being

$$\eta_{\text{pol}} = -\frac{2 \cos \iota}{1 + \cos^2 \iota} \quad (7)$$

the semi-minor to semi-major axis ratio of the polarization ellipse. In particular, $\eta_{\text{pol}} = 0$ for a linearly polarized wave and $\eta_{\text{pol}} = \pm 1$ for a circularly polarized wave, where the $+$ ($-$) sign refers to counterclockwise (clockwise) direction.

Moreover, the intrinsic signal frequency slowly decreases over time due to EM- and GW-driven rotational energy losses of the NS, which cause a secular spin-down³. The phase evolution can be expanded

¹ see <http://www.atnf.csiro.au/research/pulsar/psrcat/> for updated versions

² Third observing run of LIGO-Virgo-KAGRA [36–38] detectors that took place between April 1st 2019 and March 27th 2020 [39, 40]

³ EM-driven spin-down is usually largely dominant in known pulsars

in the NS reference frame as

$$\phi^{\text{src}}(\tau) = 2\pi \left[f_0(\tau - t_{\text{ref}}) + \frac{\dot{f}_0}{2}(\tau - t_{\text{ref}})^2 + \dots \right] + \phi_0, \quad (8)$$

where τ is the time at the source and ϕ_0 the initial phase of the signal at t_{ref} . Since the Earth moves relative to the source, the induced Doppler modulation can be described as a temporal delay between the CW arrival time at the detector, t_{arr} , and τ .

In order to remove the Doppler modulation, we must relate τ to t_{arr} such that $\phi(t_{\text{arr}}) = \phi^{\text{src}}(\tau(t_{\text{arr}}))$. Following Eq. (5) of [21], $\tau(t_{\text{arr}})$ can be written for an isolated NS as

$$\tau(t_{\text{arr}}) = t_{\text{arr}} + \frac{\vec{r}_{\text{SSB}} \cdot \vec{n}}{c} - \Delta_E - \Delta_S - \frac{D}{c}, \quad (9)$$

where the second term is the Rømer delay due to the Earth's motion, being \vec{r}_{SSB} the vector from the Solar System Barycenter (SSB) to the detector. It represents the vacuum delay between the arrival time at the observatory and the SSB. The third contribution is given by the Einstein delay (Δ_E), which takes into account the redshift due to the other solar system bodies. The term Δ_S is the Shapiro delay, linked to the deflection of a signal passing close to the Sun. The last term is the signal (light) travel time in vacuum from the source, at a distance D , to the SSB. Following [21], D/c can be neglected by redefining the intrinsic spin-down parameters.

B. Binary motion phase

The NSs in binary systems represent a more challenging target since their orbital motion induces an additional Doppler effect that must be accounted for in the analysis. The orbital motion is parameterized as a time-dependent delay added to Eq. (9),

$$\tau_{\text{bin}} = \tau(t_{\text{arr}}) - \frac{R(\tau_{\text{bin}})}{c} - \Delta_E^{\text{bin}} - \Delta_S^{\text{bin}}, \quad (10)$$

where Δ_E^{bin} and Δ_S^{bin} are, respectively, the Einstein and Shapiro delay due to the binary companion and to possible bodies in the system [43, 44]. Finally, R/c represents the Rømer delay of the binary system, with $R(\tau_{\text{bin}})$ being the radial distance of the CW-emitting NS from the *Binary Barycenter* (BB), projected along the line of sight.

Following the discussion in [21, 33], R/c can be expressed in terms of five binary orbital parameters: a_p , the projected semi-major axis along the line of sight normalised to c ; P_{orb} , the orbital period; e , the orbit eccentricity; ω , the argument of periastron;

and t_p , the time of periastron passage. Therefore, the binary delay is given by

$$\frac{R}{c} = a_p \left[\sin \omega (\cos E - e) + \cos \omega \sin E \sqrt{1 - e^2} \right], \quad (11)$$

where E is the eccentric anomaly, expressed through Kepler's equation

$$\tau_{\text{bin}} - t_p = \frac{P_{\text{orb}}}{2\pi} (E - e \sin E). \quad (12)$$

In the regime $a_p \ll P_{\text{orb}}$, which is normally the case for the observed systems, we can use the additional approximation of $E(\tau_{\text{bin}}) \approx E(t)$ as the change in E during the time R/c will be negligible. As a consequence, defining $t \equiv \tau(t_{\text{arr}})$, $E(t)$ becomes

$$t - t_p \approx \frac{P_{\text{orb}}}{2\pi} (E - e \sin E). \quad (13)$$

Moreover, since eccentricity tends to be dissipated with time [45], it is useful for relatively old binary pulsars to expand Eq. (11) in the small eccentricity regime up to the leading order in e . The binary Rømer delay can be written as [33]

$$\frac{R}{c} \approx a_p \left[\sin \psi(t) + \frac{\kappa}{2} \sin 2\psi(t) - \frac{\eta}{2} \cos 2\psi(t) - \frac{3}{2} \eta \right], \quad (14)$$

where η, κ represent the *Laplace-Lagrange* parameters, and $\psi(t)$ is the mean anomaly measured with respect to the time of ascending node t_{asc} . Defining the mean orbital angular velocity $\Omega = 2\pi/P_{\text{orb}}$, the mentioned parameters can be expressed as

$$\kappa = e \cdot \cos \omega, \quad \eta = e \cdot \sin \omega, \quad (15)$$

$$\psi(t) = \Omega (t - t_{\text{asc}}), \quad t_{\text{asc}} = t_p - \frac{\omega}{\Omega}. \quad (16)$$

III. TARGET SELECTION

Our analysis was carried out on a subset of pulsars in binary systems from version 1.70 of the ATNF catalogue [46]. We selected targets for which the NS spin period reference time was within the O3 run and for which all the binary orbital parameters are measured. The first selection criterion is justified to avoid less precise and potentially incorrect extrapolated values of the source parameters. A list of our selected targets and their parameters of interest is given in Tab. I.

The ephemerides are obtained by fitting the Time of Arrival (ToA) of photons emitted by a pulsar. To do so, astronomers exploit a time model that, in the case of pulsars in binary system, is constituted either

by $(a_p, P_{\text{orb}}, e, \omega, t_p)$, or $(a_p, P_{\text{orb}}, \eta, \kappa, t_{\text{asc}})$ when the eccentricity is small.⁴

IV. ANALYSIS METHOD

Since the binary delay correction can strongly depend on the orbital parameters, a slight offset from the true values can rapidly lead to a substantial loss of phase-coherence, with a consequent loss of SNR (see, e.g., [33]). For this reason, a semi-coherent approach, where the uncertainties on the parameters are used to determine the maximal time duration over which phase coherence can be maintained, can overcome the potential computational burden represented by a multi-template search. On the other hand, semi-coherent methods are less sensitive w.r.t. fully-coherent searches (see Eqs. (72-73) from [49]) as

$$\frac{h_{\text{sens}}^{(\text{coh})}}{h_{\text{sens}}^{(\text{semi-coh})}} \simeq \left(\frac{T_{\text{FFT}}}{T_{\text{obs}}} \right)^{1/4} \quad (17)$$

which is $\sim 23\%$ for $T_{\text{obs}} = 1$ yr and $T_{\text{FFT}} = 1$ d. This rough estimate does not consider further parameters, such as the number of selected outliers and the adopted detection statistics, upon which the sensitivity also depends (see e.g. [49]).

We propose a semi-coherent search method which makes use of calibrated and cleaned detector data preprocessed through the *Band Sampled Data* [50] (BSD) framework. The method is structured as follows: for each target, we first perform a Doppler correction in the time domain with the ephemeris central values, and then we divide the data into half-interlaced chunks of duration T_{FFT} , the so-called coherence time: its evaluation, based on the binary parameters and their uncertainties, is a crucial step of this analysis that we detail in Sec. IV A. Each chunk is windowed to reduce the finite length effect and then Fourier transformed. The next step is the selection of the local maxima from the equalized spectrum⁵ of the Fourier-transformed chunk [49, 51]: a frequency bin of this spectrum is selected only if

its height exceeds a threshold $\theta_{\text{thr}} = 2.5$. As demonstrated in [49], θ_{thr} is linked to the False Alarm Probability (FAP) per chunk p_0 through the relation

$$p_0 = e^{-\theta_{\text{thr}}} - e^{-2\theta_{\text{thr}}} + \frac{1}{3}e^{-3\theta_{\text{thr}}}, \quad (18)$$

that, for our threshold, corresponds to a value of $\approx 7.6\%$.

After that, those selected peaks along the observing run are collected together in a time-frequency map that we call *peakmap*.

The peakmap is then projected onto the frequency axis and the loudest peak around the expected frequency, in the range $f_0 \pm 1.5\delta f$ ⁶ is selected as a *candidate*, where δf is the Fourier transform frequency resolution given by

$$\delta f = \frac{1}{T_{\text{FFT}}}. \quad (19)$$

Then the *Critical Ratio* (CR), which is our detection statistics [49], is evaluated for the chosen candidates as

$$CR = \frac{x - \mu}{\sigma}, \quad (20)$$

where x is the candidate's number of counts in the projection of the peakmap (i.e. the number of times in which that specific bin has been selected), μ and σ are, respectively, the peakmap projection's average and standard deviation calculated outside the region from which the loudest peak is selected. The CR is then used to assess the statistical relevance of the candidate. As discussed in [49], $\theta_{\text{thr}} = 2.5$ is a typical value used in all-sky searches that represents a compromise among a small sensitivity loss ($\sim 10\%$), maximising the *CR* in the presence of a signal and being robust against disturbances.

An example of a peakmap before and after applying the Doppler correction is shown in Fig. 1, where a *Software Injection* (SIs, i.e. simulated signal) was performed in LIGO Livingston (LL) O3 real data.

A. Coherence time evaluation

The frequency shift due to the orbital motion can be linked to the time derivative of Eqs. (11-14) as [21]

$$\frac{\Delta f_{GW}^{\text{Doppl}}}{f_{GW}}(t) = \frac{\dot{R}}{c}(t), \quad (21)$$

⁴ For reproducibility, we refer that the ATNF ephemerides mistakenly reported some parameters. We found, in the reference paper [47], seven pulsars for which the ATNF t_p was, instead, the t_{asc} : J1811-0624, J1813-0402, J1824-0621, J1912-0952, J1929+0132, J2001+0701, J2015+0756. While for an eighth pulsar, J2338+4818, the t_p value was reported as t_{asc} [48].

⁵ The equalized spectrum is the ratio between the squared modulus of the Fourier-transformed chunk and the average single-sided *Power Spectral Density* [50].

⁶ The choice of 1.5 bins around f_0 is done after systematics studies with injections

Name	P_{orb} [day]	a_p [lt-s]	e/η^*	ω [deg] / κ^*	t_p [MJD]	t_{asc} [MJD]	f_0 [Hz]
J1326-4728B	0.08961121(1)	0.021455(7)	$1(6)\cdot 10^{-4^*}$	$-4(6)\cdot 10^{-4^*}$	-	58768.037243(4)	417.37366625(1)
J1701-3006G	0.77443355(5)	0.620316(8)	$6.1(3)\cdot 10^{-4^*}$	$6.7(3)\cdot 10^{-4^*}$	-	58894.966321(3)	434.0181102(12)
J1801-0857B	59.836454(1)	33.87543(1)	$3.82258(7)\cdot 10^{-2}$	302.1086(6)	54757.72304(9)	-	69.0569857338(2)
J1811-0624	9.38782916(5)	6.561124(2)	$-3.8(5)\cdot 10^{-6^*}$	$-2.61(12)\cdot 10^{-5^*}$	-	58692.1778781(8)	482.429490052(2)
J1813-0402	10.560352898(4)	9.4263516(5)	$-2.91(17)\cdot 10^{-6^*}$	$-2.97(12)\cdot 10^{-6^*}$	-	58716.88174915(15)	487.02569177524(4)
J1823-3021G	1.54013654(5)	3.00331(2)	$3.80466(6)\cdot 10^{-1}$	146.721(1)	58909.681498(8)	-	328.337491175(2)
J1824-0621	100.91365361(5)	44.103911(2)	$-22.809(2)\cdot 10^{-5^*}$	$-2.363(2)\cdot 10^{-5^*}$	-	58734.9698712(18)	618.61737095733(4)
J1835-3259B	1.19786323(1)	1.430841(6)	$-2.7(4)\cdot 10^{-5^*}$	$-2.2(3)\cdot 10^{-5^*}$	-	58866.2655109(6)	1092.7211722859(2)
J1912-0952	29.4925321(5)	5.379447(7)	$-1.62(18)\cdot 10^{-5^*}$	$4.6(3)\cdot 10^{-5^*}$	-	58685.963815(4)	79.78283667171(8)
J1929+0132	9.265037044(4)	8.2675144(6)	$-8.12(18)\cdot 10^{-6^*}$	$-2.44(18)\cdot 10^{-6^*}$	-	58757.4798650(2)	311.61302742043(4)
J2001+0701	5.22708263(2)	2.23028000(15)	$-1.85(12)\cdot 10^{-5^*}$	$1.29(12)\cdot 10^{-5^*}$	-	58754.681385(11)	293.25691384168(5)
J2015+0756	6.456719142(2)	5.1642574(2)	$-1.3(1)\cdot 10^{-6^*}$	$2.80(13)\cdot 10^{-6^*}$	-	58780.4740740(2)	462.10892181919(18)
J2338+4818	95.25536(2)	117.58572(7)	$1.8237(9)\cdot 10^{-3}$	99.65(2)	58868.444(7)	-	16.84774472985(17)

Table I. List of selected targets from the 1.70 ATNF catalogue version. The reference epoch for the spin frequencies is set to the Modified Julian Date (MJD) 58754.5. Starred values refer to the low-eccentricity parameters η and κ , see Eq. (15), used during the analysis. A description of the binary orbital parameter is given in Sec. II B.

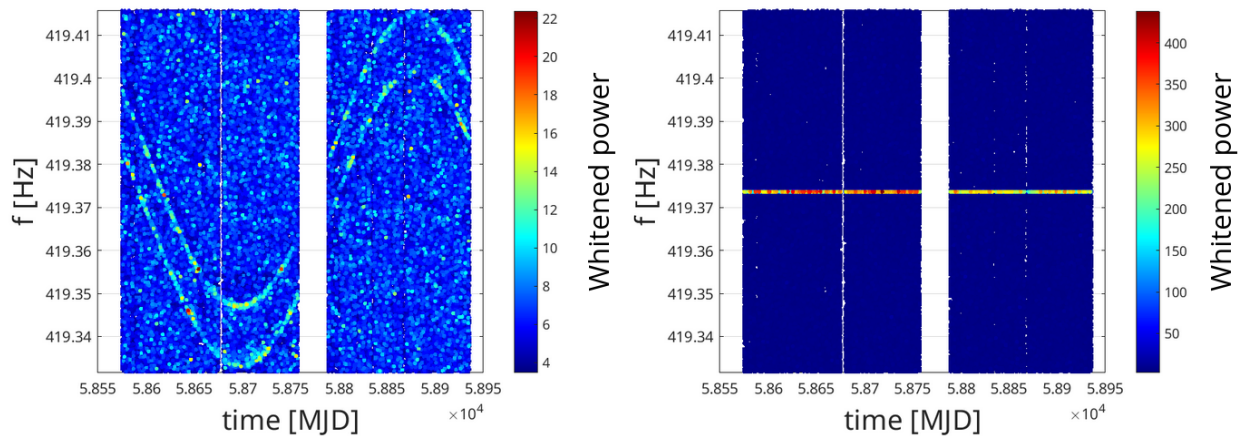


Figure 1. Peakmaps of a fake signal injected with $h_0 = 10^{-24}$ into real LL data from the O3 run over a timespan of ~ 1 yr, without (*left*) and with (*right*) the Doppler correction. The signal mimics that expected from J1326-4728B, i.e., with the same binary orbital parameters and the same sky position, while the injected frequency is $f_{GW} = 2f_{rot} + 2$ Hz to avoid the overlap with a possible true signal.

where $\Delta f_{GW}^{\text{Doppl}}$ is the time-dependent difference between the binary modulated frequency (i.e., the signal frequency after removing only the Doppler modulation due to the source sky location) and $f_{GW} = f_0 + \dot{f}_0(t - t_{\text{ref}})$. On the other hand, the right-hand side term is

$$\frac{\dot{R}}{c} = a_p \Omega \frac{\cos \omega \cos E \sqrt{1 - e^2} - \sin \omega \sin E}{1 - e \cos E}, \quad (22)$$

where we E is evaluated with Eq. (13) and we have not considered time derivatives of the orbital parameters, as their variations are typically negligible on the characteristic observing run's duration of

$$T_{\text{obs}} \sim 1 \text{ yr}^7.$$

In the limit of low eccentricities, Eq. (22) can be expressed as [33]

$$\frac{\dot{R}}{c} \approx a_p \Omega (\cos \psi + \kappa \cos 2\psi + \eta \sin 2\psi). \quad (23)$$

We evaluate the coherence time of the targets, $T_{\text{FFT}}^{\text{bin}}$, requiring that the maximum⁸ frequency shift caused by uncertainties on the Doppler correction (i.e., the variation of $\Delta f_{GW}^{\text{Doppl}}$ with respect to the

⁷ In Eq. (21) we omitted the binary Einstein and Shapiro contribution, although they are used to demodulate the data.

⁸ selected along the observation time

parameters) must be confined in half of a single frequency bin.

We calculate the residual Doppler modulation as

$$\delta\Delta f_{GW}^{\text{Doppl}}(t) \simeq f_{GW} \cdot \sum_{i=1}^5 \left. \frac{\partial \dot{R}/c}{\partial x_i} \sigma_{x_i} \right|_{x_i=x_0}, \quad (24)$$

where we omitted the time dependence of the right-hand side for simplicity. x_i are the orbital parameters (see Sec. III and Tab. I), σ_{x_i} their uncertainties, and x_0 their central values as given in the ephemerides. For the sake of completeness, we detail the calculation of Eq. (24) in App. A.

The coherence time of each source can then be estimated as

$$\max \left(\left| \delta\Delta f_{GW}^{\text{Doppl}}(t) \right| \right)_{t \in T_{\text{obs}}} \leq \frac{\delta f}{2}, \quad (25)$$

where δf is given in Eq. (19). Eq. (25) is assuming that the dominant uncertainties are coming from the orbital parameters only. In App. D we verify and show that our sources are indeed in this regime. We neglect the error on frequencies, which are typically well constrained (see Tab. I).

Finally, in the left plot of Fig. 2, we report the $T_{\text{FFT}}^{\text{bin}}$ of the targets in Tab. I calculated with Eq. (25). We do not evaluate $\delta\Delta f_{GW}^{\text{Doppl}}(t)$ using a squared sum as it would not capture potential anti-correlation among the orbital parameters, conservatively lowering the coherence time. For those targets for which the high eccentricity parameters are given (see Tab. I), our estimation with Eq. (24) is higher up to a factor of 5 than the squared sum calculation, being less conservative and potentially more sensitive. This choice is supported by the tests in Sec. IV D that did not highlight strong SNR losses linked to the offset in the orbital parameters. On the other hand, when the low eccentricity parameters are given, our coherence time estimation is up to a factor 1.8 lower than the squared sum ones, meaning that we are more conservative in that scenario at the price of sensitivity loss (see Eq. (17)).

Although in this work we describe and apply a semi-coherent approach, the coherence time calculation shows that a fraction of targets can be safely studied with a single-template fully-coherent approach as $T_{\text{FFT}}^{\text{bin}} > T_{\text{obs}}^{O3} \sim 1$ yr.

However, T_{FFT} cannot be longer than about one sidereal day⁹ as a dedicated semi-coherent technique

for the peakmap that includes the S_{FFT} statistic [52] has just been developed for the isolated pulsars science case. When T_{FFT} approaches T_{sid} , a CW monochromatic signal is split into five peaks at $f_0 \pm k/T_{\text{sid}}$, with $k = 0, 1, 2$, due to the harmonic components of the beam pattern function [41], with a significant loss in the sensitivity if not kept into account. Empirically and in agreement with generic all-sky searches [8], we observe that if $T_{\text{FFT}} > T_{\text{sid}}/5$ (see App. B) we are already sensitive to a signal power spread due to the Earth’s motion and, consequently, encounter a loss in the signal detection probability. For this reason, the present analysis is conservatively performed with a maximum coherence time equal to

$$T_{\text{FFT}}^{\text{max}} = \frac{1}{5} \cdot T_{\text{sid}} \approx 17230 \text{ s}, \quad (26)$$

for all our targets, since $T_{\text{FFT}}^{\text{bin}} > T_{\text{FFT}}^{\text{max}}$ (see Fig. 2), without the need to take into account the splitting linked to the sidereal modulation. In App. C we identify the existence in the ATNF catalogue of an additional population of potential targets, not included in the present analysis, that can benefit from this method having $T_{\text{FFT}}^{\text{bin}} < T_{\text{FFT}}^{\text{max}}$.

We stress that, although we could not reach the estimated coherence times, shorter T_{FFT} times are always more reliable against the offset in the orbital parameter and stochastic processes such as glitches [34] or accretion-induced spin-wandering [35]. In that sense, our method is complementary to full-coherent ones that exploit a grid [25] or not [24] around the measured parameters, or parallel to other semi-coherent pipelines such as [20]. In addition to that, the peculiarity of this work is that it allows to perform a single Doppler correction at the ephemeris central parameters. This is computationally very convenient compared with other pipelines [20], where a grid around the estimated values is built to probe the parameter space. Indeed, if σ_{par} (i.e., the uncertainty on a binary orbital parameter) is taken as a grid step, an interval of $\pm n_\sigma \sigma_{par}$ around each parameter becomes challenging even for small n_σ , since in each dimension we would explore in the worst case $(2n_\sigma + 1)$ values. Hence, since the dimensionality of the binary parameter space is 5, the total number of points would be $N_{grid} = (2n_\sigma + 1)^5$ values. Finer grids will be even more computationally challenging to scale towards larger pulsar datasets.

B. Sensitivity estimation

Following the conservative sensitivity estimation of [49], we can evaluate the expected minimum de-

⁹ The sidereal day represents the time taken by Earth to complete a full rotation around its rotational axis with respect to the stars. $T_{\text{sid}} \sim 86164$ s.

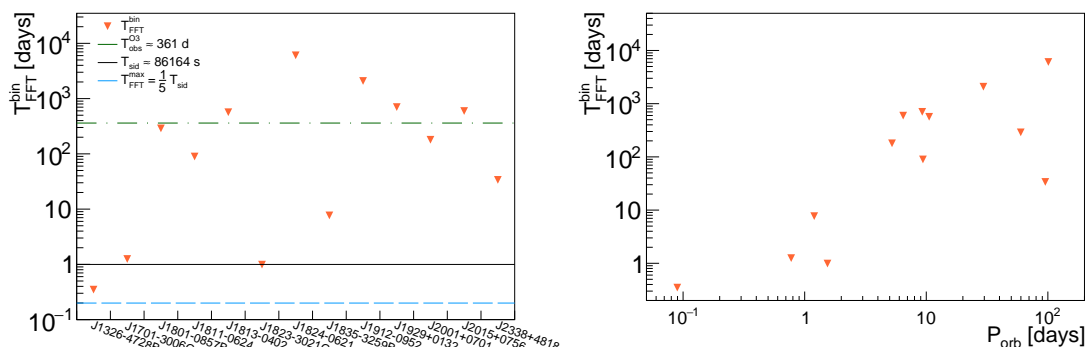


Figure 2. (left) Coherence time of each of the targets reported in Tab. I according to Eq. (25). The sidereal day duration as well as the O3 duration are reported for comparison as the solid black line and dashed-dotted green one, respectively. The dashed one is the upper value of $\frac{1}{5} \cdot T_{\text{sid}}$ used in this work to avoid the five peaks splitting. (right) Coherence times plotted against the orbital period of the targets.

teachable strain (at a given Confidence Level Γ , CL),

which would produce a candidate in a fraction $\geq \Gamma$ of a large number of repeated experiments, as

$$h_{\text{sens}} \approx \frac{4.02}{N_{\text{FFT}}^{1/4} \varepsilon^{1/4} \theta_{\text{thr}}^{1/2}} \sqrt{\frac{S_n(f)}{T_{\text{FFT}}}} \left(\frac{p_0(1-p_0)}{p_1^2} \right)^{1/4} \sqrt{CR_{\text{thr}} - \sqrt{2} \operatorname{erfc}^{-1}(2\Gamma)} \propto \left(\frac{1}{T_{\text{obs}} T_{\text{FFT}}} \right)^{1/4}, \quad (27)$$

where $S_n(f)$ is the unilateral noise spectral density,

$$p_1 = e^{-\theta_{\text{thr}}} - 2e^{-2\theta_{\text{thr}}} + e^{-3\theta_{\text{thr}}}, \quad (28)$$

p_0 is given in Eq. (18), ε is the duty cycle of the considered detector [53], and $\operatorname{erfc}(x)$ is the complementary error function defined as $\operatorname{erfc}(x) = \frac{2}{\sqrt{\pi}} \int_x^{+\infty} e^{-t^2} dt$. The curves presented throughout this paper consider $CR_{\text{thr}} \approx 2.79$, which comes from a chosen FAP in the case of white noise only of the 1% (see App. E), $\theta_{\text{thr}} = 2.5$ [49], $\Gamma = 95\%$, and the number of chunks N_{FFT} is given by

$$N_{\text{FFT}} = \frac{T_{\text{obs}}}{T_{\text{FFT}}}. \quad (29)$$

Since h_{sens} is proportional to $(T_{\text{obs}} \cdot T_{\text{FFT}})^{-1/4}$, the higher the T_{FFT} , the better is the sensitivity. Hence, longer coherence times are preferred to shorter ones.

C. Follow-up of potential outliers

Outliers are identified when their CR exceeds the threshold CR_{thr} . In such circumstances, the

peakmap is checked to discard potential correlation with a terrestrial noise. At the same time, we examine a list of known instrumental disturbances [54] to verify that no overlap between the two is present.

In the scenario where these tests are passed, we identify two potential pipelines to follow up the candidates while taking care of uncertainties in the orbital parameters.

The first follow-up method [55, 56] has the flexibility to be used in both fully- or semi-coherent mode and can take care of all the uncertainties as well. It is based on a Monte Carlo Markov Chain (MCMC), where the template bank is not fixed by a grid but rather randomly sampled according to a posterior probability. In a recent work [57], important warnings and features of this pipeline have been highlighted. Spin-wandering effects or unknown glitches would be easily tackled by this pipeline that does not require phase coherence among the segments (similarly to the method presented in this work).

For all the outliers that would not be discarded by the previous pipeline, we identify a second method [25] that can follow-up the candidates with a full-coherent approach. Here, a grid either in the orbital parameter and potentially also in the source position is explored around the measured parameters. This verification method is independent w.r.t.

the other, making it perfect to either confirm the detection¹⁰.

While the latter is based on the signal model explained in Sec. II, the former searches for a CWs using the \mathcal{F} -statistic formulation [58].

D. Test on injected signals

The computational efficiency of our new method relies on a single Doppler correction applied to each target, without the need to scan across a grid in parameter space set by the uncertainty on orbital parameters.

As a test, we simulate gapless Gaussian noise data with $T_{\text{obs}} = 365$ d and $\sqrt{S_n} = 10^{-23}/\sqrt{\text{Hz}}$ where we inject a signal that mimics the signal emitted by the targets in Tab. I.

Each SI is injected with fixed h_0 calculated with Eq. 27 for $CR = 5$ and $\Gamma = 95\%$, then we use $\cos \iota = 1$ and $\Psi = 30^\circ$, in order to circumscribe our test to the orbital parameters only. Other three couples of values are shown in App. F.

The validity is estimated employing the ratio r between the critical ratio obtained with the exact Doppler correction (On Target, OT) and when an offset d is introduced, namely

$$r(d) = \frac{CR_{\text{OFF}}}{CR_{\text{OT}}}, \quad (30)$$

where d is

$$d = \sqrt{\sum_{i=1}^5 \left(\frac{x_i^{\text{corr}} - x_i^{\text{inj}}}{\sigma_{x_i}} \right)^2}, \quad (31)$$

and represents the Euclidian distance between the parameters used for the correction and the injected ones, normalised to their uncertainties.

In the test, we calculate $r(d)$ for each target varying the parameters by adding to the central value $[\pm 1, \pm 2]\sigma_{x_i}$ ¹¹.

As expected, the uncertainties are not playing a central role (see top left plot in Fig. 3 for J1823-3021G) due to the fact $T_{\text{FFT}} < T_{\text{FFT}}^{\text{bin}}$ (see Fig. 2).

However, we made a further test on a subset of three pulsars (J1326-4728B, J1701-3006G, and J1823-3021G) as an additional step of the method's

validation. Here, we artificially vary the uncertainties given in the ephemerides to test different regimes:

- $T_{\text{FFT}}^{\text{bin}} \gg T_{\text{FFT}}^{\text{max}}$,
- $T_{\text{FFT}}^{\text{bin}} \sim T_{\text{FFT}} \ll T_{\text{FFT}}^{\text{max}}$,
- $T_{\text{FFT}}^{\text{bin}} < T_{\text{FFT}}$,

where we shrink/enlarge the uncertainties by a factor of 20. For simplicity, we show in Fig. 3 the results for J1823-3021G only as the behaviour is similar for all the targets.

We observe that in the regime $T_{\text{FFT}} < T_{\text{FFT}}^{\text{bin}}$ (top left plot of Fig. 3), there is not a loss of CR associated with the introduced offset.

More interesting are the other two regimes (bottom plots of Fig. 3), where the validity of the method is properly tested. In fact, we observe that, depending on the combination of parameters, a significant reduction of CR occurs if the length of the T_{FFT} is not chosen according to Eq. (25) as in the bottom right plot of Fig. 3. On the other hand, when the coherence time is tuned appropriately as in the bottom left plot of Fig. 3, we observe a more reduced loss that is enhanced by larger offsets as one can expect. We stress that the loss that we are showing in Fig. 3 might be overestimated because is evaluated with steps of σ_{x_i} .

We can conclude that tuning the coherence time according to the uncertainties on the orbital parameters allows for a single Doppler correction performed with the ephemeris central values. In this way, we are already sensitive to CW signals without the need for a grid in the orbital parameters thus saving computing time at a reasonable sensitivity loss.

V. RESULTS

In this section, we apply the search method to both LL and LIGO Hanford (LH) O3 real data [59]. Virgo and KAGRA data are not included systematically in the analysis as their sensitivities are, almost for all the bands, worse. We considered Virgo data only for pulsar J2338+4818, since at low frequencies its sensitivity is comparable with that of LH.

Based on the test with the SIs reported in Sec. IV D, for the targets considered here, we can safely perform a single Doppler correction at the ephemeris central values.

The threshold to identify potentially interesting outliers has been set at $CR_{\text{thr}} \sim 2.79$. In this work, we found one outlier with $CR > CR_{\text{thr}}$, see Fig. 4, for pulsar J2338+4818, for which the astrophysical origin has been confidently discarded. The outlier is due to a clear persistent excess power, linked to

¹⁰ If full-coherence can not be reached, this pipeline can analyse coherently a subset of the run to check the presence of the signal

¹¹ A smaller offset is expected in the real scenario since it is unlucky to have all the real parameters outside a $\pm\sigma_{x_i}$ interval from the measured values

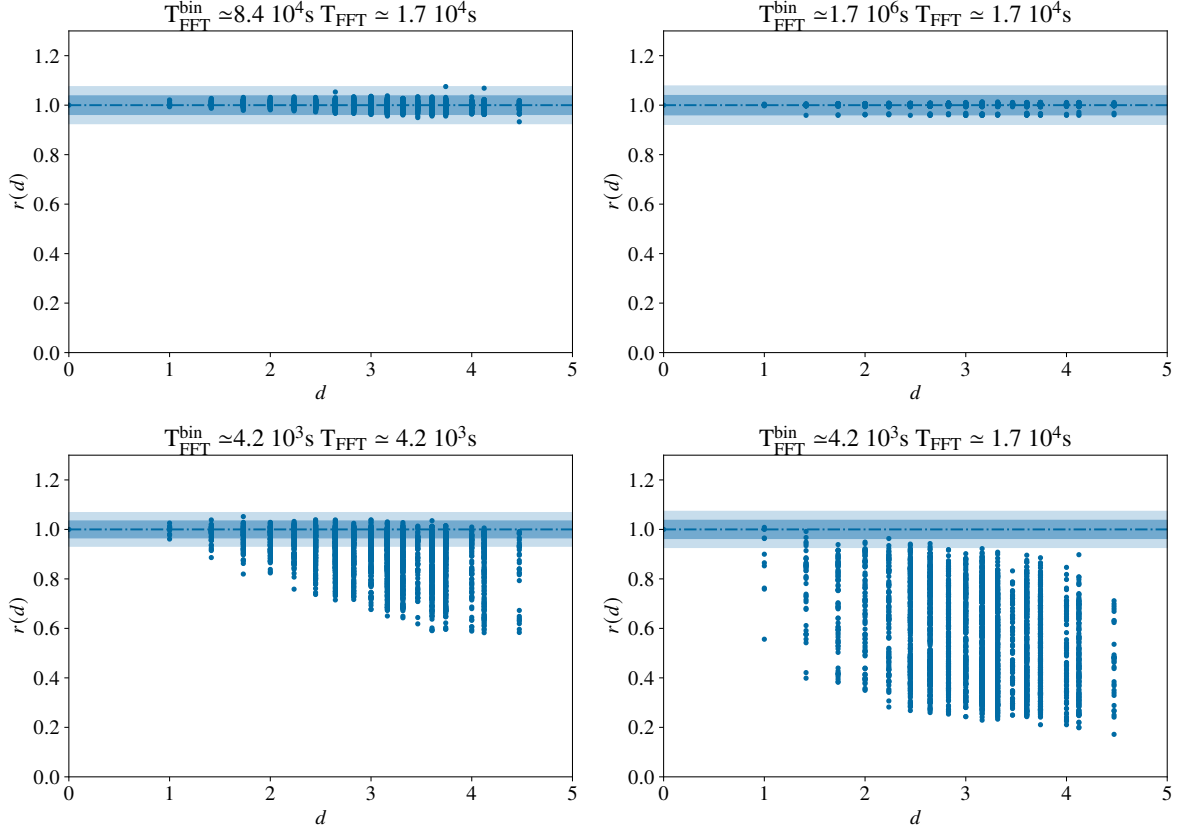


Figure 3. $r(d)$ (Eq. (30)) as a function of d (Eq. (31)) calculated with injections for pulsar J1823-3021G in simulated Gaussian noise data of $T_{\text{obs}} = 1$ yr evaluated for the nominal uncertainties (*top left*), for smaller error (*top right*) and larger (*bottom row*) by a factor of 20 w.r.t. Tab. I. $T_{\text{FFT}}^{\text{bin}}$ is the coherence time calculated with Eq. (25), while T_{FFT} is the actual coherence time used in the analysis. Each dot represents a Doppler correction performed at the distance d , the shaded region denotes a fluctuation of one (darker blue) and two (light blue) σ of the noise in the projection of the peakmap around an average $CR_{\text{OT}} \approx 27$ (FAP essentially null, see App. E). See text for details.

a calibration line. This can be seen comparing the peakmap with and without the Doppler correction, see Fig. 5.

The procedure to select a candidate is as in Sec. IV but since no CW-related one has been found, we computed the Upper Limits (ULs) for all the pulsars through an injection campaign in LL and LH data.

The calculation proceeds similarly as in [60] with the difference that we incorporate the binary modulation. We inject one by one a set of 100 SIs into the LL and LH full O3 data with a frequency ± 5 bins away from the target's one, and we start from a strain amplitude of $H_0 = h_{\text{sens}}/2$. The factor 1/2 accounts for the fact that the UL for a specific pulsar can be underneath the sensitivity curve as Eq. (27) is averaged over all sky position and CW parameters [49]. Following the test method (see Sec. IV), we inject each SI with random orbital parameters taken from Gaussians around the ephemeris central values, while the Doppler correction is performed with

the central ones. As previously mentioned, the frequency of the SIs is taken to be outside the signal region (i.e., the region where the candidate's peak is selected) to avoid overlap. If 95% of the signals are not producing $CR \geq CR_{\text{thr}}$ ¹², another set of SIs is injected with a strain increased by $h_{\text{sens}}/10$. This process is repeated till the condition is satisfied, and, in that case, the UL for the single detector is found to be

$$h_{\text{UL}}^{\text{idet}} \approx 1.31 \cdot H_{0\text{UL}}^{\text{idet}}, \quad (32)$$

being $H_{0\text{UL}}^{\text{idet}}$ the H_0 single detector's UL, while the factor 1.31 comes from averaging h_0 as a function of H_0 (i.e., inversion of Eq. (4)) over a flat $\cos \iota$ distribution. Then, we choose the highest UL between

¹² In the case of the outlier in LL data, the UL is calculated with the measured CR

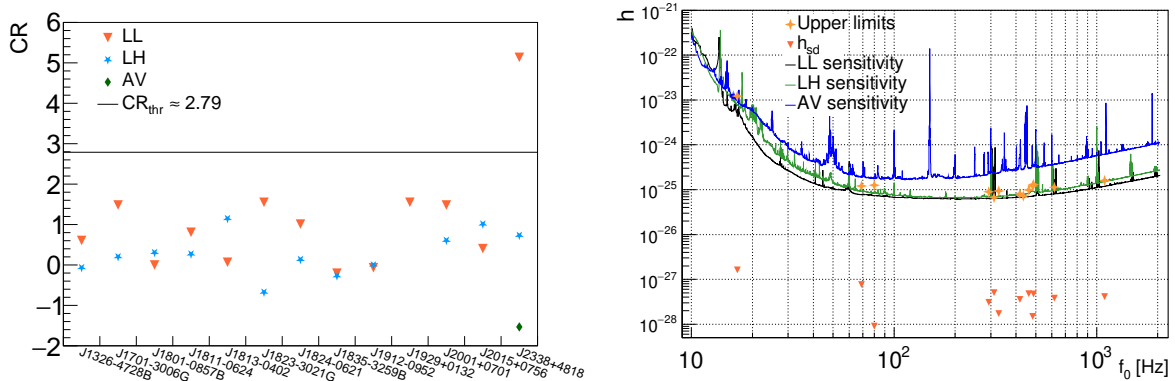


Figure 4. (*left*) Critical ratio obtained for each of the targets reported in Tab. I after performing the Doppler correction at the ephemeris central values. The AV refers to the results obtained with Virgo data. One outlier, i.e. $CR > CR_{thr}$, have been found for pulsar J2338+4818 that has been discarded (see text for a deeper discussion). (*right*) ULs on the target strains calculated through the injection of fake signals at the 95% CL in real data (ocher diamonds). The ULs are compared with the spin-down limits (see Eq. (33)) of the targets (orange triangles), and the estimated sensitivity curves are calculated with Eq. (27).

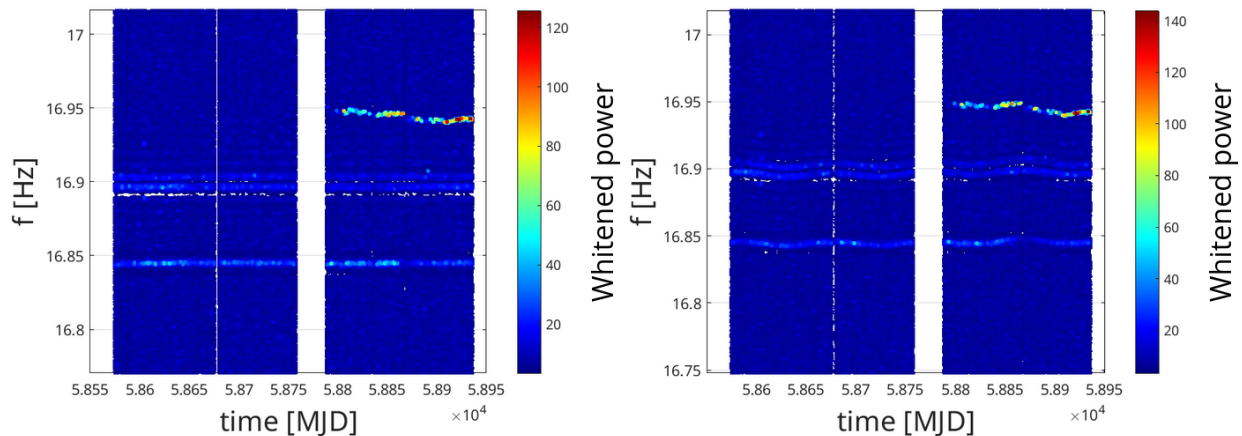


Figure 5. Peakmaps of the LL detector before (*left*) and after (*right*) Doppler correction for the pulsar J2338+4818. The search highlighted an outlier (see Fig. 4) that is likely to be of instrumental origin, due to a persistent line at $f \sim 16.85$ Hz.

the two detectors as the UL for the single target. Our ULs are presented on the right of Fig. 4 and are compared with the expected sensitivity curves for LL and LH (see Eq. (27)) and the spin-down limit defined as

$$h_{sd} = \frac{1}{D} \sqrt{\frac{5G}{4c^3} I_{zz} \left| \frac{\dot{f}_0}{f_0} \right|} \quad (33)$$

for a NS with moment of inertia $I_{zz} = 10^{38}$ kg m².

VI. CONCLUSION

In this paper, we have described a new semi-coherent method that is highly computationally effi-

cient to search for CW signals from known pulsars in binary systems. These targets can be more challenging to study as the binary Doppler correction can rapidly change within the binary orbital parameter uncertainties, potentially reducing the SNR.

The efficiency of the method here shown is a combination of two aspects: a custom optimization of the coherence time to reduce the power loss; and a single Doppler correction to assess the presence of a signal, drastically reducing the needed computational cost.

Independently on the method, our coherence time calculation can be of crucial relevance for future targeted searches where NS in binary systems are involved. With our calculation, we have given a quan-

titative estimate to understand whether a pulsar can be safely studied with a single-template fully coherent approach or a grid has to be built around the orbital parameters.

The coherence time is evaluated with the ephemeris binary orbital parameters and their uncertainties, requiring that the variation of the Doppler effect must be confined in half of a frequency bin. Applying this method to thirteen targets from the ATNF catalog version 1.70, we found coherence times that span several orders of magnitudes, from ~ 0.4 d, up to ~ 15 yr.

Before applying the method, we tested its reliability with injections in simulated data of realistic duration. Additional tests confirmed how crucial the choice of the coherence time length can be.

In order to achieve better sensitivities longer coherence times are needed. We have already foreseen crucial improvements from the software side that will overcome the sidereal day that is now limiting the present one.

By applying the method to look for a real CW coming from the selected targets, we have found one outlier that we assessed to be of terrestrial origin. We then computed upper limits on the gravitational wave strain amplitude of these targets for the very first time to our knowledge, through the injections of fake signals into real data.

Appendix A: Binary Doppler variation

As described in Sec. IV, our coherence time calculation relies on the variation of the orbital Doppler modulation expressed by Eq. (24). Here we detail its calculation.

As mentioned in Sec. III, ephemerides are given with either the parameters $(a_p, P_{\text{orb}}, e, \omega, t_p)$, or $(a_p, P_{\text{orb}}, \eta, \kappa, t_{\text{asc}})$.

Let us now focus singularly on each of the cases.

1. Low eccentricity regime

We use the low eccentricity approximation (see Eq. (14)) whenever η , κ and t_{asc} are given or the eccentricity is lower than 0.1 [33]. Since in the for-

mer scenario η , κ and t_{asc} are calculated using other parameters (see Eqs. (15-16)), the Doppler variation will have to keep that into account.

Let us start from the common term given by the derivative of Eq. (23) with respect to a_p

$$\frac{\partial \dot{R}/c}{\partial a_p} = \frac{1}{a_p} \cdot \frac{\dot{R}}{c}. \quad (\text{A1})$$

Considering the scenario where the lagrangian parameters are given, the contributions from the other parameters are calculated as

$$\frac{\partial \dot{R}/c}{\partial P_{\text{orb}}} = \frac{1}{P_{\text{orb}}} \left(a_p \Omega \psi (\sin \psi + 2\kappa \sin 2\psi - 2\eta \cos 2\psi) - \frac{\dot{R}}{c} \right), \quad (\text{A2})$$

$$\frac{\partial \dot{R}/c}{\partial t_{\text{asc}}} = a_p \Omega^2 (\sin \psi + 2\kappa \sin 2\psi - 2\eta \cos 2\psi), \quad (\text{A3})$$

$$\frac{\partial \dot{R}/c}{\partial \eta} = a_p \Omega \sin 2\psi, \quad (\text{A4})$$

$$\frac{\partial \dot{R}/c}{\partial \kappa} = a_p \Omega \cos 2\psi. \quad (\text{A5})$$

The contributions are calculated differently if e , ω , t_p are given

$$\frac{\partial \dot{R}/c}{\partial P_{\text{orb}}} = -\frac{1}{P_{\text{orb}}} \left(a_p \Omega (\omega - \psi) (\sin \psi + 2\kappa \sin 2\psi - 2\eta \cos 2\psi) + \frac{\dot{R}}{c} \right), \quad (\text{A6})$$

$$\frac{\partial \dot{R}/c}{\partial t_p} = \frac{\partial \dot{R}/c}{\partial t_{\text{asc}}}, \quad (\text{A7})$$

$$\frac{\partial \dot{R}/c}{\partial e} = a_p \Omega (\cos 2\psi \cos \omega + \sin 2\psi \sin \omega), \quad (\text{A8})$$

$$\frac{\partial \dot{R}/c}{\partial \omega} = -a_p \Omega (\sin \psi + 2\kappa \sin 2\psi - 2\eta \cos 2\psi). \quad (\text{A9})$$

2. High eccentricity regime

On the other hand, the Doppler variation in the high eccentricity regime is calculated by exploiting the following contributions

$$\frac{\partial \dot{R}/c}{\partial E} = \frac{a_p \Omega (\sin \omega (e - \cos E) - \cos E \sin \omega \sqrt{1 - e^2})}{(1 - e \cos E)^2} \quad (\text{A10})$$

$$\frac{\partial \dot{R}/c}{\partial P_{\text{orb}}} = -\frac{\Omega}{P_{\text{orb}}} \frac{\partial \dot{R}/c}{\partial E} \frac{t - t_p}{1 - e \cos E}, \quad (\text{A11})$$

$$\frac{\partial \dot{R}/c}{\partial t_p} = -\frac{\Omega}{1 - e \cos E} \frac{\partial \dot{R}/c}{\partial E}, \quad (\text{A12})$$

$$\begin{aligned} \frac{\partial \dot{R}/c}{\partial e} = & \frac{\sin E}{1 - e \cos E} \frac{\partial \dot{R}/c}{\partial E} + \frac{a_p \Omega}{(1 - e \cos E)^2} \left(\cos E \left(\frac{\cos E - e}{\sqrt{1 - e^2}} \cos \omega - \sin \omega \sin E \right) + \right. \\ & \left. + \sin^2 E \frac{\sin \omega (e - \cos E) - \cos \omega \sin E \sqrt{1 - e^2}}{\sin E - \cos E (E - \Omega (t - t_p))} \right), \end{aligned} \quad (\text{A13})$$

$$\frac{\partial \dot{R}/c}{\partial \omega} = \frac{a_p \Omega}{1 - e \cos E} (\sin \omega \cos E \sqrt{1 - e^2} + \cos \omega \sin E). \quad (\text{A14})$$

As expressed in Eq. (24), the Doppler variation consists of the sum of the terms listed in this appendix, weighted by the uncertainty on each parameter.

Appendix B: Upper bound to the coherence time

The current implementation of the method presented in Sec. IV does not account for the Earth’s rotational Doppler modulation. Due to the harmonic components of the beam pattern function [41], the power of the monochromatic CW is split into up to five components at $f_0 \pm k/T_{sid}$, with $k = 0, 1, 2$, limiting the coherence time of a search if not correctly kept into account.

Since the relative height of the harmonics is not constant but rather depends on the detector and source locations [58], the splitting is not uniform and rules the number of peaks found above the noise level.

We set the highest coherence time of the search by studying the worst-case scenario, where the splitting is almost even among the harmonics. In the top part of Fig. 6 we show the power spectrum of the *Hardware Injection*¹³ (HI) 1 and an isolated NS SI, where five and four harmonics are visible respectively after removing all the Doppler modulation except the sidereal one. We analyse both the signals with different coherence time in $T_{\text{FFT}} \in [0.02 T_{sid}, T_{sid}]$ with a step of $0.05 T_{sid}$. The bottom plot in Fig. 6 shows the CR obtained with each of the T_{FFT} values. We observe a decreasing trend for both the SI and HI1 that starts around $T_{\text{FFT}} \sim 0.2 T_{sid}$ confirming this effect can significantly reduce the detection chances if not properly accounted for. For this reason, we set $0.2 T_{sid}$ as our highest coherence time.

	HI 1	SI
α	37.39°	121.98°
δ	-29.45°	-21.49°
f_0 [Hz]	848.937	101.217
\dot{f}_0 [Hz/s]	$-3 \cdot 10^{-10}$	0
h_0	$1.68 \cdot 10^{-24}$	$2.74 \cdot 10^{-25}$
$\cos \iota$	0.46	0.34
Ψ	20.40°	-28.60°

Table II. Injection parameters of the signals shown in Fig. 6. The frequency reference time is given at $t_{\text{ref}} = 58574$ MJD.

Appendix C: Coherence time of ATNF pulsars in binary systems

We selected from the ATNF catalogue the pulsars in binary systems using the python package `psrqpy` [61] applying the same criteria described in Sec. III without the requirement on the frequency reference time. In Fig. 7 we show the histogrammed $T_{\text{FFT}}^{\text{bin}}$ that we obtained from these targets with Eq. (25). Our estimation highlights a non-null population of pulsars (31 out of 235) with $T_{\text{FFT}}^{\text{bin}} < T_{\text{FFT}}^{\text{max}}$.

Appendix D: Uncertainties on sky location

Although in this work we focused on uncertainties on the orbital parameters, the sky position indetermination can play in principle a non-negligible role. Here we present an “equivalent” coherence time calculation based on [49].

Following Eqs. (38-42) of [49] we can link the resolution in the sky parameters¹⁴ to the T_{FFT}

$$T_{\text{FFT}}^{\text{sky}}(\delta\lambda) \approx \frac{10^4}{f_0 \delta\lambda \cos \beta}, \quad T_{\text{FFT}}^{\text{sky}}(\delta\beta) \approx \frac{10^4}{f_0 \delta\beta \sin \beta}, \quad (\text{D1})$$

¹³ CW injected through the detector hardware for testing purposes, see [here](#) for the injection parameters

¹⁴ We make use of the ecliptic coordinates λ and β

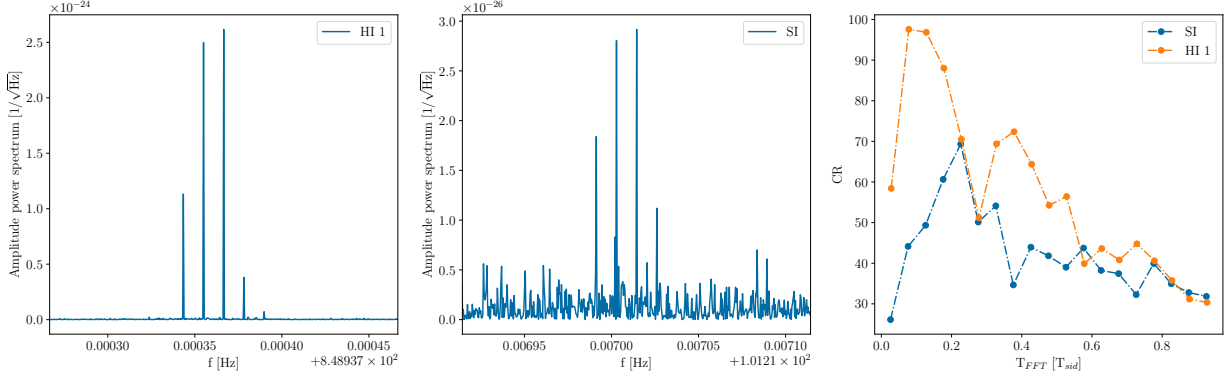


Figure 6. Power spectra of the HI 1 (*left*) and a SI (*middle*) for which the 5 harmonics of the signals are visible, see Tab. II for the injection parameters. (*right*) CR as a function of the coherence time. Too high values tend to disperse the signal power, lowering the significance of the candidate.

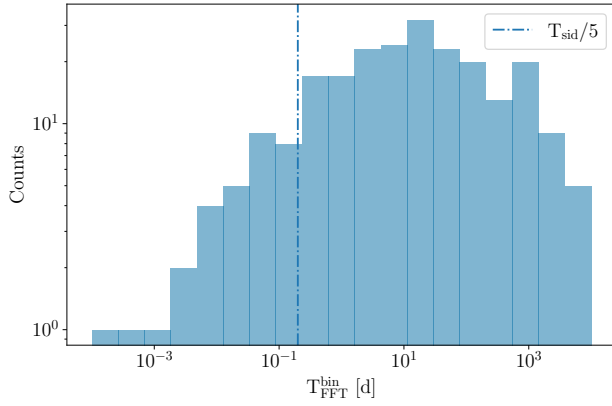


Figure 7. Histogrammed $T_{\text{FFT}}^{\text{bin}}$ of 235 ATNF binary pulsars calculated with Eq. (25).

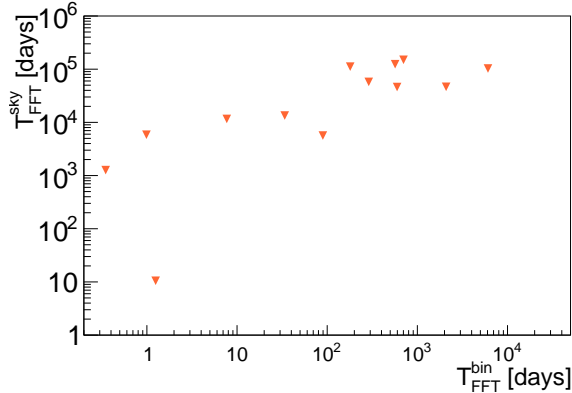


Figure 8. Coherence time given by uncertainties on sky location (Eq. (D1)) plotted against the $T_{\text{FFT}}^{\text{bin}}$ given by the uncertainties on binary parameters (Eq. (25)).

where 10^4 is approximately the inverse ratio of the

Earth’s orbital velocity and c . Here we are interpreting $\delta\lambda$ and $\delta\beta$ as the uncertainties on the sky location given by astronomers.

The comparison of $\min(T_{\text{FFT}}^{\text{sky}}(\delta\lambda), T_{\text{FFT}}^{\text{sky}}(\delta\beta))$ (i.e., the worst-case scenario between the two) with the T_{FFT} from Eq. (25) allows to determine whether the binary orbital uncertainties are dominating over the others. For this reason, considering the values reported in Tab. III for each of our targets, in Fig. 8 we plot the coherence time calculated with the two sets of uncertainties one against the other. As we can see, $T_{\text{FFT}}^{\text{sky}}$ is greater than the other estimation by a factor of $O(10^{1-3})$ depending on the considered target.

Name	β [°]	$\delta\beta$ [°]	$\delta\lambda$ [°]
J1326-4728B	-35.23433	$1.3 \cdot 10^{-5}$	$1.5 \cdot 10^{-5}$
J1701-3006G	-7.3218	$1.1 \cdot 10^{-2}$	$4 \cdot 10^{-4}$
J1801-0857B	14.479409	$6 \cdot 10^{-6}$	$1.7 \cdot 10^{-6}$
J1811-0624	17.000105	$8 \cdot 10^{-6}$	10^{-6}
J1813-0402	19.3503669	$3 \cdot 10^{-7}$	10^{-7}
J1823-3021G	-7.02626	$1.4 \cdot 10^{-5}$	$3 \cdot 10^{-6}$
J1824-0621	16.9408957	$4 \cdot 10^{-7}$	10^{-7}
J1835-3259B	-9.786669	$3 \cdot 10^{-6}$	$5 \cdot 10^{-7}$
J1912-0952	12.424092	$4 \cdot 10^{-6}$	$1.8 \cdot 10^{-6}$
J1929+0132	23.0986161	$3 \cdot 10^{-7}$	$1.5 \cdot 10^{-7}$
J2001+0701	26.9071496	$3 \cdot 10^{-7}$	$2 \cdot 10^{-7}$
J2015+0756	26.9623559	$4 \cdot 10^{-7}$	$3 \cdot 10^{-7}$
J2338+4818	45.264334	$4 \cdot 10^{-6}$	$4 \cdot 10^{-5}$

Table III. Ecliptic latitude β and uncertainties on sky location used to evaluate Eq. (D1) for each of the targets in Tab. I.

We leave as a future work the estimation of the coherence time based on the thorough variation of the Doppler modulation. It would be eventually needed wherever the two evaluations (Eqs. (25)-(D1)) are

comparable. As for now, we would suggest considering a gridded approach separately on the two sets of parameters or rather discarding the target.

Appendix E: CR noise distribution

Here we detail the FAP calculation at a given CR_{thr} .

In the absence of signals, the peakmap consists of frequency bins selected according to a binomial distribution [49] with probability equal to p_0 (see Eq. (18)) and number of trials $2N_{\text{FFT}}$, with the factor of 2 due to the half-interlaced FFTs.

We are interested in the distribution followed by the maximum CR over $N_{\text{bin}} = 3$ bins since we select the loudest frequency bin within $f_0 \pm 1.5 \delta f$, see Sec. IV. As a result, the FAP can be estimated through the relation

$$\text{FAP}(CR_{\text{thr}}) = (\text{cdf}[B_N(x_{\text{thr}}, 2N_{\text{FFT}}, p_0)])^{N_{\text{bin}}} \quad (\text{E1})$$

with B_N indicating the binomial distribution described above, and cdf its cumulative distribution function evaluated at

$$x_{\text{thr}}(CR_{\text{thr}}) = CR_{\text{thr}} \cdot \sigma + \mu \quad (\text{E2})$$

that is Eq. (20) inverted. The CR_{thr} corresponding to a fixed FAP value can then be estimated through root-finding algorithms.

We show in Fig. 9 between the FAP estimated through Eq. (E1) and simulations.

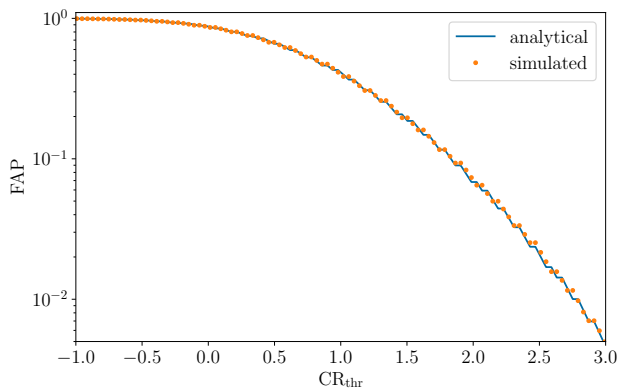


Figure 9. FAP evaluated with Eq. (E1) (solid blue line) compared with simulated gapless, Gaussian noise-only data (orange dots) for $T_{\text{obs}} = 1$ yr and $T_{\text{FFT}} = 17236$ s.

Appendix F: Additional tests

As a further test, we performed the same study described in Sec. IV with other values of $\cos \iota$ and

Ψ . For simplicity, we show in Fig. 10 the outcome of the systematic study with errors enlarged by a factor of 20 with three additional combination of the two parameters.

Comparing bottom left plot of Fig. 3 with the first two plots of Fig. 10 ($\cos \iota = \pm\sqrt{2}/2$), we observe the same trend of r as a function d . The right plot of Fig. 10, where $\cos \iota = 0$, shows a similar pattern but presenting larger fluctuations, linked to the lower CR s involved (due to a fainter projected strain H_0 , see Eq. (4)).

ACKNOWLEDGMENT

We would like to thank the PRD reviewer for fruitful comments that improved this work.

This research has made use of data or software obtained from the Gravitational Wave Open Science Center (gwosc.org), a service of the LIGO Scientific Collaboration, the Virgo Collaboration, and KAGRA. This material is based upon work supported by NSF's LIGO Laboratory which is a major facility fully funded by the National Science Foundation, as well as the Science and Technology Facilities Council (STFC) of the United Kingdom, the Max-Planck-Society (MPS), and the State of Niedersachsen/Germany for support of the construction of Advanced LIGO and construction and operation of the GEO600 detector. Additional support for Advanced LIGO was provided by the Australian Research Council. Virgo is funded, through the European Gravitational Observatory (EGO), by the French Centre National de Recherche Scientifique (CNRS), the Italian Istituto Nazionale di Fisica Nucleare (INFN) and the Dutch Nikhef, with contributions by institutions from Belgium, Germany, Greece, Hungary, Ireland, Japan, Monaco, Poland, Portugal, Spain. KAGRA is supported by Ministry of Education, Culture, Sports, Science and Technology (MEXT), Japan Society for the Promotion of Science (JSPS) in Japan; National Research Foundation (NRF) and Ministry of Science and ICT (MSIT) in Korea; Academia Sinica (AS) and National Science and Technology Council (NSTC) in Taiwan.

We would like to acknowledge CNAF for providing the computational resources.

We would like to also acknowledge the ATNF Pulsar Catalogue, R. N. Manchester, R. N. Manchester, G. B. Hobbs, A. Teoh & M. Hobbs, *Astronomical Journal*, 129, 1993-2006 (2005), see <http://www.atnf.csiro.au/research/pulsar/psrcat> for updated versions.

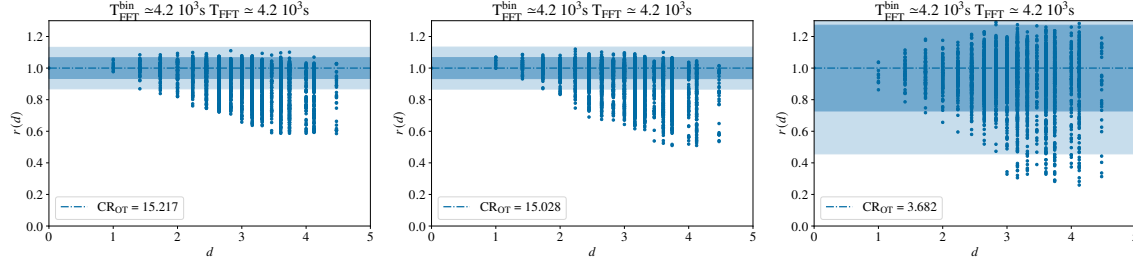


Figure 10. Same as bottom left plot in Fig. 3. Here signals are injected with (left) $\cos \iota = \sqrt{2}/2$, $\psi = -30^\circ$, (middle) $\cos \iota = -\sqrt{2}/2$, $\psi = 30^\circ$ and (right) $\cos \iota = 0$, $\psi = 30^\circ$. Larger fluctuations are present in the $\cos \iota = 0$ plot w.r.t. the others due to the less number of counts in the projection of the peakmap.

-
- [1] B. T. Reed, A. Deibel, and C. J. Horowitz, *The Astrophysical Journal* **921**, 89 (2021).
- [2] H. Hakobyan et al., *Astrophys. J.* **943**, 105 (2023).
- [3] B. J. Owen, *Phys. Rev. Lett.* **95**, 211101 (2005).
- [4] B. Rajbhandari, B. J. Owen, S. Caride, and R. Inta, *Phys. Rev. D* **104**, 122008 (2021).
- [5] O. J. Piccinni, *Galaxies* **10**, 72 (2022).
- [6] B. P. Abbott et al. (LIGO Scientific Collaboration and Virgo Collaboration), *Phys. Rev. D* **96**, 062002 (2017).
- [7] B. P. Abbott et al. (LIGO Scientific Collaboration and Virgo Collaboration), *Phys. Rev. D* **100**, 024004 (2019).
- [8] R. Abbott et al. (LIGO Scientific Collaboration, Virgo Collaboration, and KAGRA Collaboration), *Phys. Rev. D* **106**, 102008 (2022).
- [9] B. P. Abbott et al. (LIGO Scientific Collaboration and Virgo Collaboration), *Phys. Rev. D* **94**, 102002 (2016).
- [10] B. Steltner et al., *The Astrophysical Journal* **909**, 79 (2021).
- [11] B. Steltner et al., *The Astrophysical Journal* **952**, 55 (2023).
- [12] B. P. Abbott et al. (LIGO Scientific Collaboration and Virgo Collaboration), *Phys. Rev. D* **96**, 122004 (2017).
- [13] V. Dergachev and M. A. Papa, *Phys. Rev. X* **13**, 021020 (2023).
- [14] V. Dergachev and M. A. Papa, *Phys. Rev. D* **109**, 022007 (2024).
- [15] E. Goetz and K. Riles, *Classical and Quantum Gravity* **28**, 215006 (2011).
- [16] R. Abbott et al. (The LIGO Scientific Collaboration and the Virgo Collaboration), *Phys. Rev. D* **103**, 064017 (2021).
- [17] P. B. Covas and A. M. Sintes, *Phys. Rev. Lett.* **124**, 191102 (2020).
- [18] P. B. Covas, M. A. Papa, R. Prix, and B. J. Owen, *The Astrophysical Journal Letters* **929**, L19 (2022).
- [19] R. Abbott et al. (LIGO Scientific, VIRGO, KAGRA), *Astrophys. J.* **935**, 1 (2022).
- [20] R. Abbott et al. (LIGO Scientific Collaboration, Virgo Collaboration, and KAGRA Collaboration), *Phys. Rev. D* **105**, 022002 (2022).
- [21] P. Leaci et al., *Phys. Rev. D* **95**, 122001 (2017).
- [22] J. T. Whelan et al., *The Astrophysical Journal* **949**, 117 (2023).
- [23] R. Abbott et al., *The Astrophysical Journal Letters* **941**, L30 (2022).
- [24] L. D’Onofrio et al., *Phys. Rev. D* **108**, 122002 (2023).
- [25] A. Singhal et al., *Class. Quant. Grav.* **36**, 205015 (2019).
- [26] B. P. Abbott et al. (LIGO Scientific Collaboration and Virgo Collaboration), *Phys. Rev. D* **96**, 122006 (2017).
- [27] B. P. Abbott et al. (LIGO Scientific Collaboration and Virgo Collaboration), *Phys. Rev. Lett.* **120**, 031104 (2018).
- [28] R. Abbott et al. (LIGO Scientific Collaboration, Virgo Collaboration, and KAGRA Collaboration), *Phys. Rev. D* **106**, 042003 (2022).
- [29] B. P. Abbott et al. (LIGO Scientific Collaboration and Virgo Collaboration), *Phys. Rev. D* **95**, 082005 (2017).
- [30] A. Ashok et al., *The Astrophysical Journal* **923**, 85 (2021).
- [31] C. J. Clark et al., *Monthly Notices of the Royal Astronomical Society* **519**, 5590 (2023), ISSN 0035-8711.
- [32] L. Nieder et al., *The Astrophysical Journal Letters* **902**, L46 (2020).
- [33] P. Leaci and R. Prix, *Phys. Rev. D* **91**, 102003 (2015).
- [34] G. Ashton, R. Prix, and D. I. Jones, *Phys. Rev. D* **96**, 063004 (2017).
- [35] A. Mukherjee, C. Messenger, and K. Riles, *Phys. Rev. D* **97**, 043016 (2018).
- [36] LIGO Scientific Collaboration, *Classical and Quantum Gravity* **32**, 074001 (2015).
- [37] F. et al, *Classical and Quantum Gravity* **32**, 024001 (2015).
- [38] K. Somiya (KAGRA), *Class. Quant. Grav.* **29**, 124007 (2012).
- [39] M. Tse et al., *Phys. Rev. Lett.* **123**, 231107 (2019).

- [40] F. Acernese et al. (Virgo Collaboration), *Phys. Rev. Lett.* **123**, 231108 (2019).
- [41] P. Jaranowski and A. Królak, *Phys. Rev. D* **61**, 062001 (2000).
- [42] J. Abadie et al., *The Astrophysical Journal* **737**, 93 (2011).
- [43] G. B. Hobbs, R. T. Edwards, and R. N. Manchester, *Monthly Notices of the Royal Astronomical Society* **369**, 655 (2006), ISSN 0035-8711.
- [44] R. T. Edwards, G. B. Hobbs, and R. N. Manchester, *Monthly Notices of the Royal Astronomical Society* **372**, 1549 (2006), ISSN 0035-8711.
- [45] P. C. Peters, *Phys. Rev.* **136**, B1224 (1964).
- [46] R. N. Manchester, G. B. Hobbs, A. Teoh, and M. Hobbs, *The Astronomical Journal* **129**, 1993 (2005).
- [47] C. C. Miao et al., *Monthly Notices of the Royal Astronomical Society* **518**, 1672 (2022), ISSN 0035-8711.
- [48] M. Cruces et al., *Monthly Notices of the Royal Astronomical Society* **508**, 300 (2021), ISSN 0035-8711.
- [49] P. Astone et al., *Phys. Rev. D* **90**, 042002 (2014).
- [50] O. J. Piccinni et al., *Class. Quant. Grav.* **36**, 015008 (2019).
- [51] P. Astone, S. Frasca, and C. Palomba, *Classical and Quantum Gravity* **22**, S1197 (2005).
- [52] S. D'Antonio et al., *Phys. Rev. D* **108**, 122001 (2023).
- [53] R. Abbott et al. (KAGRA, VIRGO, LIGO Scientific), *Astrophys. J. Suppl.* **267**, 29 (2023).
- [54] E. Goetz et al., *O3 lines and combs in found in self-gated c01 data*, T2100201-v2, (2021).
- [55] G. Ashton and R. Prix, *Phys. Rev. D* **97**, 103020 (2018).
- [56] R. Tenorio, D. Keitel, and A. M. Sintes, *Phys. Rev. D* **104**, 084012 (2021).
- [57] L. Mirasola and R. Tenorio, :2405.18934 (2024).
- [58] P. Jaranowski, A. Królak, and B. F. Schutz, *Phys. Rev. D* **58**, 063001 (1998).
- [59] R. Abbott et al., *The Astrophysical Journal Supplement Series* **267**, 29 (2023).
- [60] B. P. Abbott et al., *The Astrophysical Journal* **882**, 73 (2019).
- [61] M. Pitkin, *Journal of Open Source Software* **3**, 538 (2018).